

Biomacromolecule-Assisted Synthesis and Electrocapacitive Behavior of Manganese Ferrite Nanoparticles

Shuibo Liu¹, Zichao Li¹, Xiao-xiong Wang², Xuehua Liu¹, Wanneng Ye^{1,*}, Yun-ze Long², Hongliang Li¹, Peizhi Guo^{1,*}, X.S. Zhao¹

¹ Institute of Materials for Energy and Environment, State Key Laboratory Breeding Based of New Fiber Materials and Modern Textile, School of Materials Science and Engineering, Qingdao University, Qingdao, 266071, P. R. China

² College of Physics, Qingdao University, Qingdao 266071, P. R. China

*E-mail: ywn@qdu.edu.cn, pzguo@qdu.edu.cn, qduguo@163.com

Received: 4 June 2017 / Accepted: 28 September 2017 / Published: 12 November 2017

Two types of manganese ferrite nanoparticles, namely MF-SA and MF-CHI, have been synthesized solvothermally from the synthesis systems containing sodium alginate and chitosan, respectively. Both MF-SA and MF-CHI showed well crystalline nature based on the XRD and TEM measurements. The larger saturation magnetization value of MF-SA should be ascribed to its slightly larger crystallite size than that of MF-CHI. Results from N₂ adsorption-desorption isotherms and Raman spectra confirmed the structural difference in MF-SA and MF-CHI. The electrocapacitive behavior of manganese ferrite-based supercapacitors has been studied and MF-SA displayed a specific capacitance of around 60.4 F•g⁻¹ at 0.25 A•g⁻¹ in aqueous symmetric supercapacitors, larger than that of MF-CHI about 45.1 F•g⁻¹ at the same condition. MF-SA based supercapacitor also showed better capacitance maintenance of around 82% of the initial value at 1 A•g⁻¹ after 2000 cycle test than that of MF-CHI based cells. Based on the experimental data, the structure-property relationship of two types of MnFe₂O₄ nanoparticles have been discussed and analyzed.

Keywords: Ferrite, Nanoparticle, Marine biomolecule, Raman spectroscopy, Supercapacitor

1. INTRODUCTION

Transition metal oxide materials have attracted increasing attentions in many areas (i.e. catalysis, energy storage and conversion, and biomedicine) owing to their physicochemical properties [1-7]. Element iron is the second richest metal on Earth's reserves and very cheap. Thereafter, metal oxide materials containing iron have received great attention to explore their possible applications in energy storage and conversion [8,9]. On the one hand, various iron oxides have been used, such as,

either as the active electrode materials for lithium iron batteries and supercapacitors [8-14] or as the optical-electrocatalysts for water splitting [15-17]. For example, iron oxide nanostructures obtained either by quasiemulsion-template method or from metal-organic frameworks can be used as the active electrode materials for electrochemical devices [18,19]. On the other hand, double or triple metal oxides containing iron, such as spinel ferrites, have also gained more and more attention to be used in energy and environmental fields [20,21]. For instance, nickel ferrite displayed better catalytic activity in photocatalytic water oxidation than single metal oxide, namely nickel oxide or iron oxide [21].

Diverse ferrite nanostructures including nanoparticles [22,23], hollow structures [24], nanorods [25] nanowires [26], and nanotubes [27] have been prepared by the application of various methods including template [28], thermolysis [29], co-precipitation [30], sol-gel technique [31] and solvothermal method [32]. Recently, ferrite nanostructures has been used as the electrode materials for aqueous solution based electrochemical supercapacitors [33,34]. It is reported that supercapacitors based on ferrite colloidal nanocrystal assemblies displayed electrocapacitive performance, which can be adjusted by the structure of ferrite nanostructures as well as the nature of electrolytes used [34-36]. However, the electrochemical behavior of ferrite nanoparticles remains to be further clarified.

Biological macromolecules are the basic substances of life. Sodium alginate and chitosan are two typical kinds of biological macromolecules with a wide range of sources and can react with metal ions via coordination interactions. Usually, sodium alginate, as one kind of natural polysaccharide, is a by-product after extraction of iodine and mannitol from kelp or seaweed. However, chitosan can be obtained by deacetylation of chitin. Both of these polysaccharide compounds have been used in many fields, including medicine, food, cosmetics, water treatment, and biomedical engineering. In the meantime, chitosan and sodium alginate have active functional groups that can react with many kinds of metal ions [37]. In this work, two types of spinel ferrite nanoparticles have been synthesized via the solvothermal method based on the synthesis systems containing sodium alginate and chitosan. The structure of ferrite nanoparticles have been characterized by a series of techniques including XRD, (HR) TEM, FTIR, Raman and N₂ adsorption-desorption measurements as well as magnetic investigations at room temperature. Electrochemical experiments displayed that ferrite nanoparticles from the sodium alginate system showed a larger capacitance and cycle stabilization than those obtained from the synthesis system containing chitosan.

2. EXPERIMENTAL

2.1 Materials

All the used chemicals purchased from Sinopharm Chemical Reagent Co. were used as received (analytical grade). Ultrapure water (18.2 MΩ cm) was used for electrochemical measurements.

2.2 Synthesis of $MnFe_2O_4$ nanoparticles:

In a typical synthesis, an ethylene glycol (20 mL) solution containing $Mn(CH_3COO)_2 \cdot 4H_2O$ and $FeCl_3 \cdot 6H_2O$ was obtained homogeneously under stirring with the molar ratio of 1:2 at room temperature. Different dosages of sodium alginate or chitosan were dissolved in distilled water (10 ml). Then both of the above solutions were mixed under stirring and then transferred into a Teflon-lined stainless autoclave (40 mL). After heating at 200 °C for 12 h in an oven, the autoclave was cooled naturally down to room temperature. Then the samples were collected by repeatedly centrifugation and washing thoroughly with distilled water and ethanol, followed by dried in an oven at 60 °C for 8 h. The obtained samples are noted as MF-SA and MF-CHI, where MF represents $MnFe_2O_4$, SA and CHI represent sodium alginate and chitosan used in the preparation, respectively.

2.3 Sample characteristics

Transmission electron microscope (TEM) and high resolution TEM (HRTEM) images of the samples were recorded on a transmission electron microscope (JSM-2100F) with an operating voltage of 200 kV. The crystallographic information of the products were investigated using a Rigaku UltimaIV X-ray diffractometer (XRD, Cu-K α radiation $\lambda=0.15418$ nm). The specific surface areas were estimated with the Brunauer-Emmett-Teller (BET) method with N₂ adsorption data in the relative pressure range of $P/P_0 = 0.05-0.35$. The pore size distributions were calculated using the Barrett-Joyner-Halenda (BJH) model applied to the desorption branch of the N₂ isotherms obtained with a Quantachrome Autosorb-IQ-MP/XP surface area and pore analyzer. The thermogravimetric analysis was performed with a Mettler Toledo TGA-2 thermogravimetric analyzer under an oxygen atmosphere with a heating rate of 10 °C•min⁻¹. Magnetic properties were measured using a Physical Property Measurement System (PPMS) vibrating sample magnetometer (VSM) at room temperature. Fourier transformation infrared (FTIR) measurements were carried out with a Nicolet iS5 FTIR spectrophotometer on KBr pellets. Raman spectra were collected using a Renishaw inVia Plus Micro-Raman spectroscopy system equipped with a 50mW DPSS laser at 532 nm.

2.4 Electrochemical performance of $MnFe_2O_4$ nanoparticles

To prepare the electrode, the as-prepared samples, PTFE and acetylene carbon black were mixed in isopropyl alcohol with a ratio of 85:10:5 at room temperature. Then the mixture was pressed onto a nickel foam[36], followed by drying at 110 °C for 10h under vacuum. The loading mass of the active material in each electrode was about 4 mg. Symmetrical supercapacitors were fabricated by using two electrodes which separated by a porous membrane in 2 M KCl electrolyte. Room temperature electrochemical characterizations performed on CHI760D electrochemical workstation (CH Instruments, USA) include cyclic voltammetry (CV), galvanostatic charge-discharge (GCD), and electrochemical impedance spectroscopy (EIS) measurements.

3. RESULTS AND DISCUSSION

3.1 Morphology and nanostructure

MnFe₂O₄ nanoparticles obtained from the sodium alginate system was abbreviated as MF-SA and MF-CHI from the chitosan system. TEM and HRTEM measurements are used to investigate the morphology and crystalline features of these two samples [38]. As depicted in Fig. 1A and C, the MnFe₂O₄ nanoparticles are observed in low magnified TEM images, but not well-dispersed, with the shortest width of about 10 nm and no nanoparticles larger than 20 nm observed. The selected-area electron diffraction (SAED) patterns of both MF-SA and MF-CHI in the insets in Fig. 1A and C indicate the crystalline nature of these samples in which bright diffraction spots can be observed. Fig. 1B shows the HRTEM image of a single MF-SA nanoparticle, in which the marked lattice spacings are about 2.43 Å and 2.50 Å, ascribed to the interplanar distance of (222) and (311) lattice planes, respectively. For sample MF-CHI, the calculated lattice spacings are about 2.38 Å and 2.50 Å based on the HRTEM image shown in Fig. 1D, also in accordance with the interplanar distance of (222) and (311) planes of MnFe₂O₄ phase, respectively. The observed angles between the (222) and (311) planes are about 90° for MF-SA and MF-CHI, similar to the theoretical value.

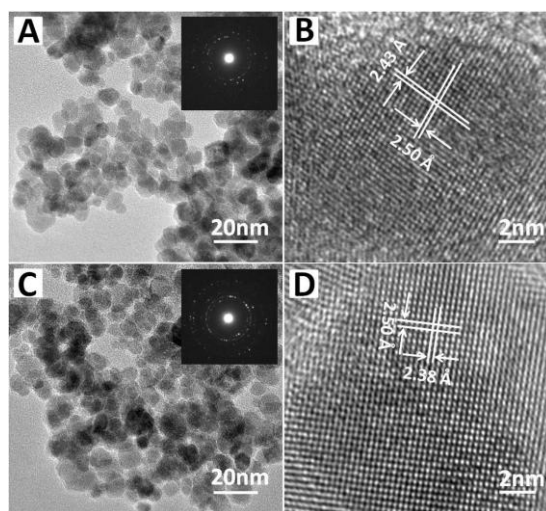


Figure 1. TEM (A, C) and HRTEM (B, D) images of MF-SA (A, B) and MF-CHI (C, D). Insets in images a and c are the corresponding SAED pattern of the sample.

The crystalline structures of both samples are also confirmed by the XRD measurements (Fig. 2). The diffraction peaks of each sample, appeared at 2θ degrees of 30°, 35°, 43°, 56°, 62°, can be well-indexed respectively to (220), (311), (400), (511) and (440) planes of cubic spinel MnFe₂O₄ (JCPDS card No. 88-1965). The observed diffraction peaks indicate the formation of small MnFe₂O₄ nanoparticles, as confirmed by the TEM measurements. The structural features of samples MF-SA and MF-CHI were further investigated by nitrogen gas sorption technique. Fig. 3A and B show the N₂ adsorption-desorption isotherms and Barrett-Joyner-Halenda (BJH) pore size distribution curves of two types of MnFe₂O₄ nanoparticles, respectively. It can be seen that the type IV physisorption nature

of two isotherms was obtained according to the IUPAC classification, which showed a typical H1-type hysteresis loop, indicating that mesoporous structures are clearly existed in these samples. The specific surface areas and total pore volumes were respectively calculated about $105.5 \text{ m}^2 \cdot \text{g}^{-1}$ and $0.23 \text{ cm}^3 \cdot \text{g}^{-1}$ for MF-SA, and $89.0 \text{ m}^2 \cdot \text{g}^{-1}$ and $0.13 \text{ cm}^3 \cdot \text{g}^{-1}$ for MF-CHI. These results would be responsible for the electrocapacitive behavior of MF-SA and MF-CHI.

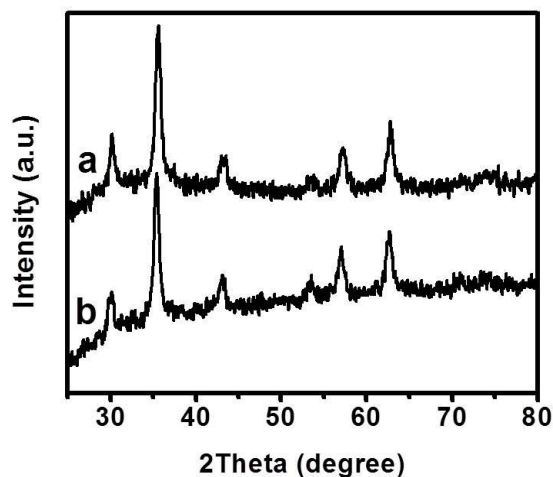


Figure 2. XRD patterns of MF-CHI (a) and MF-SA (b).

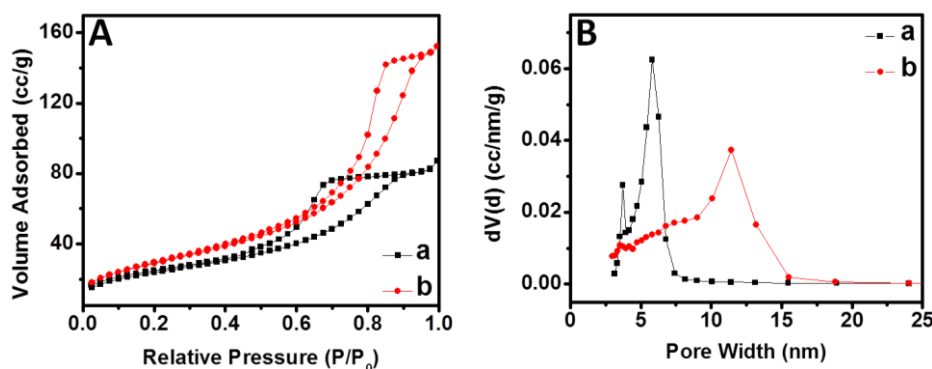


Figure 3. Nitrogen adsorption/desorption isotherms (A) and BJH pore size distributions (B) of MF-CHI (a) and MF-SA (b).

3.2 Thermogravimetry, FTIR analysis and Raman analysis

As is shown in Fig. 4, the thermogravimetric analysis (TGA) curves of both samples display several mass loss platforms, which indicates the similar mass loss processes of both samples. As depicted in Fig. 4A, the first step below $150 \text{ }^\circ\text{C}$ is related to the removal of moisture adsorbed on the surface and pores of MnFe_2O_4 nanoparticles. From $200\text{--}400 \text{ }^\circ\text{C}$, the decomposition of adsorbed organic residues on the surface of the samples during the solvothermal synthesis took place. From $500 \text{ }^\circ\text{C}$ to $800 \text{ }^\circ\text{C}$, it is the third step which is quite slow mass loss until reach a plateau at $610 \text{ }^\circ\text{C}$ corresponding to the further decomposition of the surface residuals. It is obvious that the weight loss

rate of MF-CHI (Fig. 4B) in the second step is faster than that of MF-SA (Fig. 4B), indicating more organic residuals adsorption onto the surfaces of MF-CHI nanoparticles than that of MF-SA.

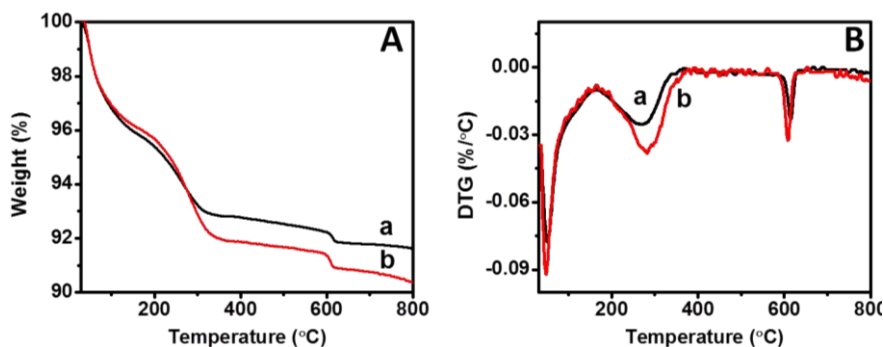


Figure 4. TGA (A) and DTG (B) curves of MF-SA (a) and MF-CHI (b).

This can be further evidenced by the FTIR measurements. Fig. 5A displays the FTIR spectra of MF-SA and MF-CHI in the range 400–4000 cm^{-1} . The broad bands at 3420 and 1637 cm^{-1} represent the stretching and bending vibrations of the O-H bond, respectively [39]. While two weak bands at 2847 and 2928 cm^{-1} are signed respectively to the CH_2 asymmetric and symmetric stretching bands. Thus, it indicates the presence of a very small amount of free or absorbed water and organic residues remaining on the surface of the samples. It is observed that two absorption bands in the 465 cm^{-1} and 580–620 cm^{-1} may be caused by the vibration of octahedral groups FeO_6 and the stretching vibration of tetrahedral groups FeO_4 , respectively. Further, the strength of the absorption peaks for MF-CHI is much stronger than that of MF-SA, indicating that these results are essentially the same as that obtained from the TGA measurements.

As is known to all, Raman scattering and infrared absorption spectra can be used to study the lattice vibration problems, and can complement each other. Fig. 5B shows the Raman spectra of in the range 200–900 cm^{-1} and both of MF-SA and MF-CHI show obvious peak in the 686 cm^{-1} , especially for MF-SA. This is due to the symmetry stretching vibration of the metal atoms and the O atoms [39]. As depicted in Fig. 5B, MF-SA nanoparticles represent three peaks at 322, 473 and 686 cm^{-1} . The peak at 686 cm^{-1} is typical of the spinel ferrite, due to the A_{1g} mode corresponding to the O atoms symmetrically stretching along the Fe-O bond at the tetrahedral locations [40–42]. Two peaks at 322 cm^{-1} and 473 cm^{-1} are respectively attributed to the E_g and T_{2g} mode corresponding to the symmetrical bending of O atoms relative to Fe and the asymmetric stretching of Fe-O bond at the tetrahedral sites. For MF-CHI, very weak signals except at 686 cm^{-1} was observed which may be ascribed to the existence of chitosan in the synthesis system, leading to the difference in crystal structure between MF-SA and MF-CHI.

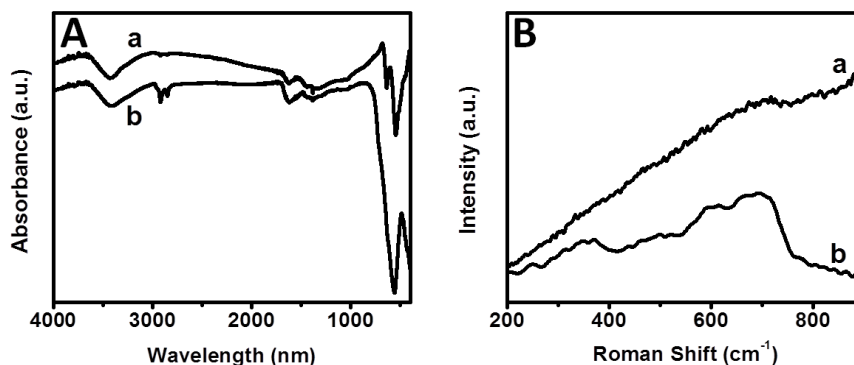


Figure 5. FTIR (A) and Raman (B) spectra of MF-CHI (a) and MF-SA (b).

3.3 Magnetic characterization

Magnetic properties of two types of MnFe_2O_4 nanoparticles were tested (Fig. 6) with the maximum magnetic field strength of $H = 1.5 \times 10^4$ Oe. Clearly, the hysteresis behavior cannot be clearly seen in the full magnetization curves (Fig. 6A). As shown in Fig. 6B, a small hysteresis loop was observed in a magnification view indicating that a weak ferromagnetic behavior was existed in MF-SA and MF-CHI. The saturation magnetization (M_s) values of MF-SA and MF-CHI were about 70.7 and 67.8 $\text{emu} \cdot \text{g}^{-1}$ with the crystallite sizes of 18 and 17 nm, respectively. The M_s values of both MF-SA and MF-CHI were much lower than 110 $\text{emu} \cdot \text{g}^{-1}$ for the reported bulk of MnFe_2O_4 [43], which were affected by many factors including crystalline nature, particle size and surface effect. It can also be seen that the remnant magnetization (M_r) and coercivity (H_c) values are 1.5 $\text{emu} \cdot \text{g}^{-1}$ and 10 Oe for MF-SA, while 0.8 $\text{emu} \cdot \text{g}^{-1}$ and 7.5 Oe for MF-CHI, respectively. These observations are in agreement with the crystalline nature as well as the surface nature of these two samples.

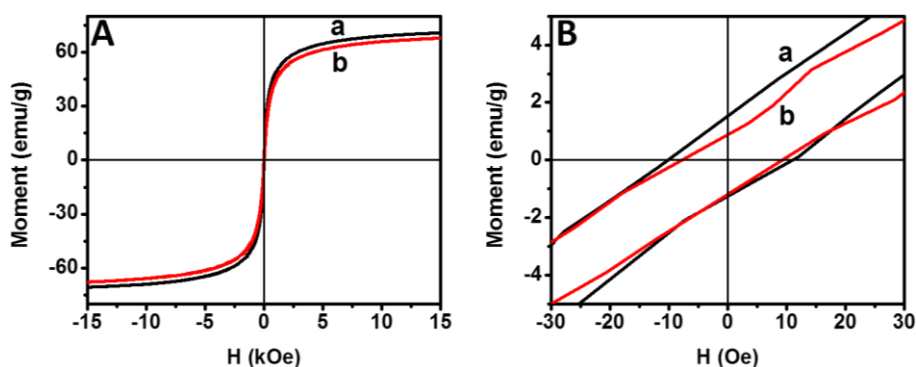


Figure 6. The magnetization hysteresis of MF-SA (a) and MF-CHI (b).

3.4 Electrochemical properties

The as-made MnFe_2O_4 nanoparticles were used to assembly two-electrode cells to explore their performance in symmetric supercapacitors [44]. Fig. 7 shows the CV curves of MF-SA and MF-CHI based supercapacitors, named SC-MF-SA and SC-MF-CHI, respectively, by using aqueous KCl (2 M) solutions as the electrolyte. Both the CV curves of SC-MF-SA and SC-MF-CHI obtained at 50 $\text{mV} \cdot \text{s}^{-1}$,

as shown in Fig. 7A, showed a symmetric rectangular shape. In the meantime, the current of the CV curve for SC-MF-SA is higher than that of SC-MF-CHI. Even if the scan rate was much increased to $500 \text{ mV}\cdot\text{s}^{-1}$, the as-obtained CV curves of SC-MF-CHI also displayed an excellent rectangular shape (Fig. 7B). Although the CV curve of SC-MF-SA collected at $500 \text{ mV}\cdot\text{s}^{-1}$ expressed a slightly distort compared with that of SC-MF-CHI, denoting the existence of a low contact resistance in both supercapacitors. All these observations demonstrated the electrocapacitive features of both types of supercapacitors. It is obvious that the currents of these two types of MnFe_2O_4 nanoparticle-based supercapacitors are slightly lower than those of MnFe_2O_4 colloidal nanocrystal assemblies, assembled by the nanoparticles with the similar particle size [36,45].

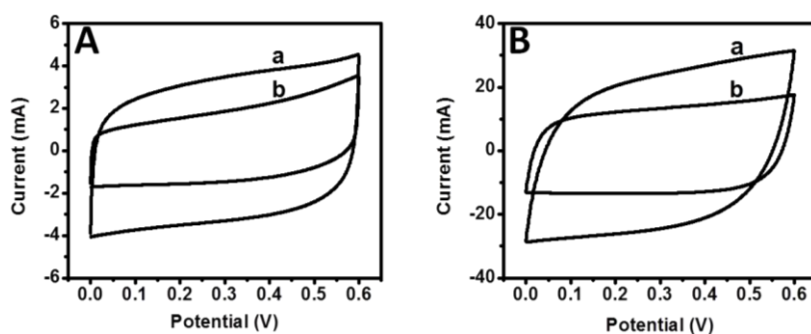


Figure 7. CV curves of SC-MF-SA (a) and SC-MF-CHI (b): A, $50 \text{ mV}\cdot\text{s}^{-1}$; B, $500 \text{ mV}\cdot\text{s}^{-1}$.

The galvanic charge-discharge characterization was further used to investigate the electrocapacitive behavior of both supercapacitors. Fig. 8A and Fig. 8B show the GCD curves of SC-MF-SA and SC-MF-CHI at varied current densities. The GCD curves of SC-MF-SA exhibited a slightly distorted triangular shape for all the collected data (Fig. 8A). As for SC-MF-CHI (Fig. 8B), the shape of GCD curves was more irregular compared with those of SC-MF-SA. In the meantime, the discharge times of SC-MF-SA at all the varied current densities were larger than those of SC-MF-CHI, indicating the existence of a higher specific capacitance for SC-MF-SA. The specific capacitances of SC-MF-SA and SC-MF-CHI under different currents were listed in Fig. 8C. It is observed that the capacitances decreased gradually from $0.15 \text{ A}\cdot\text{g}^{-1}$ to $2 \text{ A}\cdot\text{g}^{-1}$. It is obvious that the specific capacitance of the electrode material decreases with the current density increased whatever the electrolyte is. Under high current density, because the sluggish diffusion dynamics of electrolyte ions led to the low utilization rate of the electrode materials, resulting in the smaller capacitance. However, the concentration polarization is somewhat obvious at a large current density that can affect the specific capacitance of supercapacitor [35]. For SC-MF-SA, the capacitances were calculated to be about 65.2 , 60.4 and $57.2 \text{ F}\cdot\text{g}^{-1}$ at 0.15 , 0.25 , $0.5 \text{ A}\cdot\text{g}^{-1}$, respectively. The capacitance was further decreased from $53.8 \text{ F}\cdot\text{g}^{-1}$ at $0.75 \text{ A}\cdot\text{g}^{-1}$ to $50.3 \text{ F}\cdot\text{g}^{-1}$ at $1 \text{ A}\cdot\text{g}^{-1}$. The capacitance of SC-MF-SA was decreased to $46.2 \text{ F}\cdot\text{g}^{-1}$ at $2 \text{ A}\cdot\text{g}^{-1}$, about 71% of the value obtained at $0.15 \text{ A}\cdot\text{g}^{-1}$. For SC-MF-CHI, the capacitances were obviously smaller than those of SC-MF-SA. It was seen that the capacitances were 50.4 , 45.1 and $40.2 \text{ F}\cdot\text{g}^{-1}$ at 0.15 , 0.25 and $0.5 \text{ A}\cdot\text{g}^{-1}$, respectively. Namely, the capacitances were also decreased faster than those of SC-MF-SA at the same experimental conditions. Finally, the capacitance was down to $30.2 \text{ F}\cdot\text{g}^{-1}$ at $2 \text{ A}\cdot\text{g}^{-1}$, which only maintained about 60% of that obtained at $0.15 \text{ A}\cdot\text{g}^{-1}$. These

capacitances were clearly smaller than those of MnFe_2O_4 colloidal nanocrystal assemblies composed of small nanoparticles [34,36].

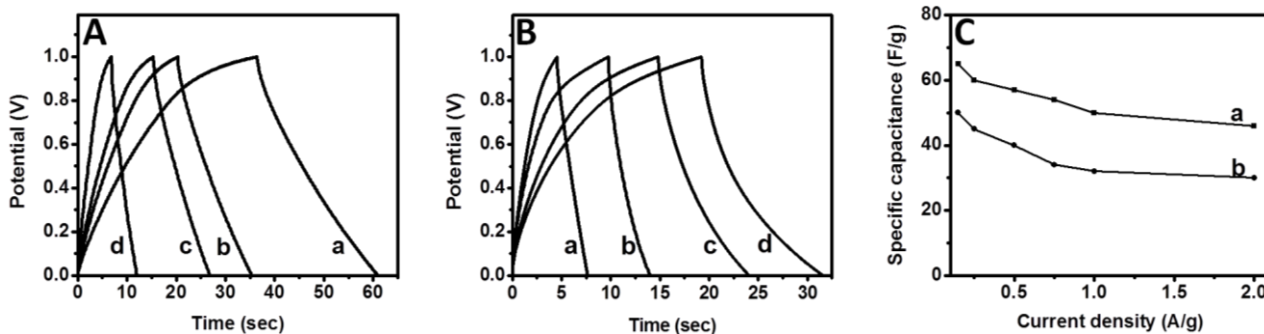


Figure 8. GCD curves of SC-MF-SA (A) and SC-MF-CHI (B) under different current densities. a) $0.5 \text{ A}\cdot\text{g}^{-1}$; b) $0.75 \text{ A}\cdot\text{g}^{-1}$; c) $1 \text{ A}\cdot\text{g}^{-1}$; d) $2 \text{ A}\cdot\text{g}^{-1}$. Variation curves (C) of the capacitances of SC-MF-SA (a) and SC-MF-CHI (b).

Based on the CV and GCD measurements, it is suggested that the nanoparticle structure of MF-SA and MF-CHI may be somewhat unpleasant to be used as the electrode materials compared with those colloidal nanocrystal assemblies [36,45]. This can also be confirmed by the cycle performance of both supercapacitors (Fig. 9). It is seen from Fig. 9A that the capacitances were decreased from 57.4 to $49.3 \text{ F}\cdot\text{g}^{-1}$ for SC-MF-SA and from 40.5 to $31.2 \text{ F}\cdot\text{g}^{-1}$ for SC-MF-CHI at 0.5 A/g , after 2000 cycles, about 86% and 77% of the initial values, respectively. If the current density was up to $1 \text{ A}\cdot\text{g}^{-1}$ (Fig. 9B), the capacitance of SC-MF-SA declined to $41.2 \text{ F}\cdot\text{g}^{-1}$ after 2000 cycles, about 82% of its original capacitance, while left about 75% for SC-MF-CHI at the same condition. These indicated that the assembly of nanoparticles should help for the cycle performance of manganese ferrite based supercapacitors.

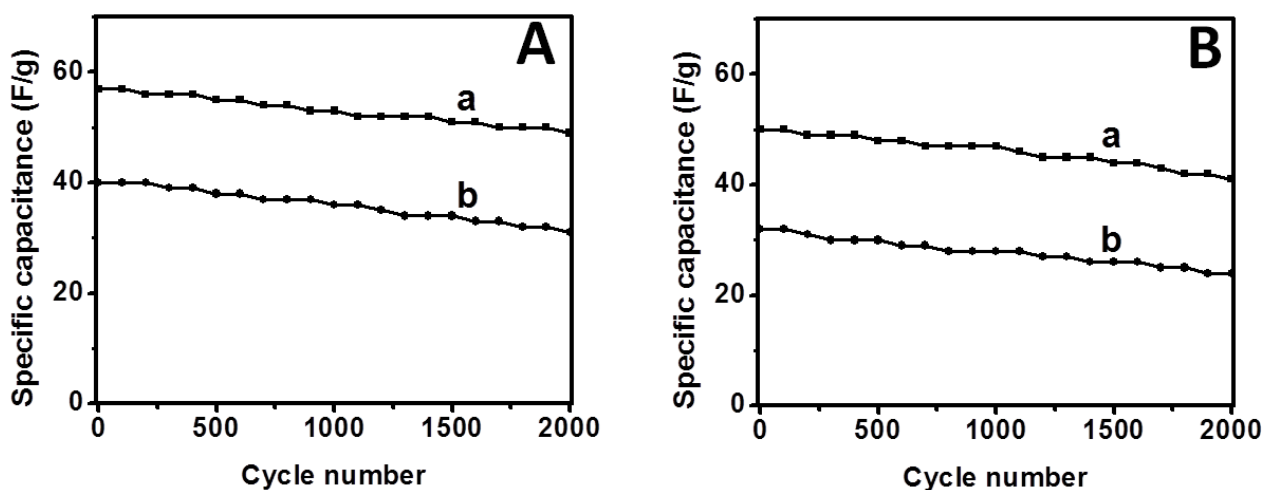


Figure 9. Cycle stability of SC-MF-SA (a) and SC-MF-CHI (b): (A) $0.5 \text{ A}\cdot\text{g}^{-1}$; (B) $1 \text{ A}\cdot\text{g}^{-1}$.

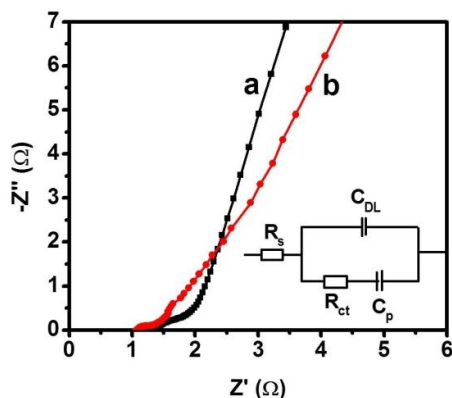


Figure 10. Nyquist plots of SC-MF-SA (a) and SC-MF-CHI (b).

To further investigate the electrode/electrolyte interface features, EIS was conducted for both supercapacitors to analyze the frequency behavior at the range of 0.01-1000 kHz and equivalent series resistance (ESR). As shown in Fig. 10, a high frequency semicircle can be observed from the Nyquist plots of the supercapacitors. In the equivalent circuit, R_s called equivalent series resistance (ESR), C_{DL} represents the electronic transfer resistance of the electrode; R_{ct} corresponds to the electron transfer resistance at the electrode/electrolyte interface; the C_p corresponds to the steep line [36]. In the meantime, a low frequency sloping line appeared simultaneously, in which the slope was increased from SC-MF-CHI to SC-MF-SA. Usually, the ideal supercapacitor has a larger slope at a lower frequency line, which also means better electrocapacitive performance. This denoted that SC-MF-SA displayed a better electrocapacitive performance than SC-MF-CHI, which was in good accordance with above results. It is suggested that the better electrochemical performances of SC-MF-SA should be attributed to the well crystalline nature, unique surface composite and structure of MF-SA compared with MF-CHI.

4. CONCLUSIONS

Biomacromolecule systems have been used to synthesize $MnFe_2O_4$ nanoparticles by using solvothermal method. $MnFe_2O_4$ nanoparticles, named as MF-SA, obtained from the system containing sodium alginate have a slightly larger crystallite size than those based on chitosan-based synthesis system (MF-CHI), MF-SA displays a larger saturation magnetization value than MF-CHI due to the less surface organic residue and larger crystallite size of MF-SA. On the basis of electrochemical measurements, the MF-SA based symmetrical supercapacitor displays better electrocapacitive behavior than that assembled by MF-CHI. These results would be help for the design and synthesis of novel $MnFe_2O_4$ nanostructures with high performances based on biomacromolecule synthesis systems.

ACKNOWLEDGMENTS

This work was financially supported by the National Natural Science Foundation of China (Nos. U1232104, 51373082 and 51673103), the Taishan Scholars Advantageous and Distinctive Discipline Program for supporting the research team of energy storage materials of Shandong Province, and the Taishan Scholars Program of Shandong Province, China (ts20120528).

References

1. J. H. Lee, J. T. Jang, J. S. Choi, S. H. Moon, S. H. Noh, J. W. Kim, J. G. Kim, I. S. Kim, K. I. Park, J. Cheon, *Nat. Nanotechnol.* 6 (2011) 418.
2. R. Hao, R. J. Xing, Z. C. Xu, Y. L. Hou, S. Gao, S. H. Sun, *Adv. Mater.* 22 (2010) 2729.
3. C. Z. Yuan, H. B. Wu, Y. Xie, X. W. Lou, *Angew. Chem., Int. Ed.* 53 (2014) 1488.
4. Q. T. Qu, S. B. Yang, X. L. Feng, *Adv. Mater.* 23 (2011) 5574.
5. M. A. Mezaal, L. M. Qu, W. Liu, G. H. Li, X. Y. Zhao, L. X. Lei, *Int. J. Electrochem. Sci.* 11 (2016) 5924.
6. P. Poizot, S. Laruelle, S. Grugeon, L. Dupont, J. M. Tarascon, *Nature* 407 (2000) 496.
7. W. Liu, P. Oh, X. Liu, M. J. Lee, W. Cho, S. Chae, Y. Kim, J. Cho, *Angew. Chem., Int. Ed.* 54 (2015) 4440.
8. M. S. Burke, M. G. Kast, L. Trotochaud, A. M. Smith, S. W. Boettcher, *J. Am. Chem. Soc.* 137 (2015) 3638.
9. S. Zhu, J. J. Li, X. Y. Deng, C. N. He, E. Z. Liu, F. He, C. S. Shi, N. Q. Zhao, *Adv. Funct. Mater.* 27 (2017) 1605017.
10. A. S. Adekunle, B. O. Agboola, K. I. Ozoemena, E. E. Ebenso, J. A. O. Oyekunle, O. S. Oluwatobi, J. N. Lekitima, *Int. J. Electrochem. Sci.* 10 (2015) 3414.
11. H. Xia, C. Y. Hong, B. Li, B. Zhao, Z. X. Lin, M. B. Zheng, S. V. Savilov, S. M. Aldoshin, *Adv. Funct. Mater.* 25 (2015) 627.
12. G. Iervolino, I. Tantis, L. Sygellou, V. Vaiano, D. Sannino, P. Lianos, *Appl. Surf. Sci.* 400 (2017) 176.
13. H. Zhou, L. S. Zhang, D. Y. Zhang, S. Q. Chen, P. R. Coxon, X. He, M. Coto, H. K. Kim, K. Xi, S. J. Ding, *Sci. Rep.* 6 (2016) 37752.
14. Y. P. Lin, N. L. Wu, *J. Power Sources* 196 (2011) 851.
15. H. L. Li, H. Liu, A. P. Fu, G. L. Wu, M. Xu, G. S. Pang, P. Z. Guo, J. Q. Liu, X. S. Zhao, *Materials* 9 (2016) 849.
16. K. Sivula, R. Zboril, F. Le Formal, R. Robert, A. Weidenkaff, J. Tucek, J. Frydrych, M. Gratzel, *J. Am. Chem. Soc.* 132 (2010) 7436.
17. Y. G. Li, X. L. Wei, X. Y. Yan, J. T. Cai, A. N. Zhou, M. R. Yang, K. Q. Liu, *Phys. Chem. Chem. Phys.* 18 (2016) 10255.
18. B. Wang, J. S. Chen, H. B. Wu, Z. Y. Wang, X. W. Lou, *J. Am. Chem. Soc.* 133 (2011) 17146.
19. D. X. Wang, A. P. Fu, H. L. Li, Y. Q. Wang, P. Z. Guo, J. Q. Liu, X. S. Zhao, *J. Power Sources* 285 (2015) 469.
20. C. Du, X. G. Yang, M. T. Mayer, H. Hoyt, J. Xie, G. McMahon, G. Bischooping, D. W. Wang, *Angew. Chem., Int. Ed.* 52 (2013) 12692.
21. D. C. Hong, Y. Yamada, T. Nagatomi, Y. Takai, S. Fukuzumi, *J. Am. Chem. Soc.* 134 (2012) 19572.
22. V. Blanco-Gutierrez, R. Saez-Puche, M. J. Torralvo-Fernandez, *J. Mater. Chem.* 22 (2012) 2992.
23. V. A. Kumary, J. Divya, T. E. M. Nancy, K. Sreevalsan, *Int. J. Electrochem. Sci.* 8 (2013) 6610.
24. J. C. Liu, Q. Z. Jiao, W. J. Cao, Y. Zhao, H. S. Li, *J. Mater. Sci.* 49 (2014) 3795.
25. N. N. Wang, H. Y. Xu, L. Chen, X. Gu, J. Yang, Y. T. Qian, *J. Power Sources* 247 (2014) 163.
26. F. Ebrahimi, F. Ashrafizadeh, S. R. Bakhshi, *J. Alloys Compd.* 656 (2016) 237.
27. H. M. Fan, J. B. Yi, Y. Yang, K. W. Kho, H. R. Tan, Z. X. Shen, J. Ding, X. W. Sun, M. C. Olivo, Y. P. Feng, *ACS Nano* 3 (2009) 2798.
28. Y. Xu, H. Wei, J. L. Yao, J. L. Fu, D. S. Xue, *Mater. Lett.* 62 (2008) 1403.
29. N. Z. Bao, L. M. Shen, Y. H. A. Wang, J. X. Ma, D. Mazumdar, A. Gupta, *J. Am. Chem. Soc.* 131 (2009) 12900.

30. R. R. Liu, M. Lv, Q. B. Wang, H. L. Li, P. Z. Guo, X. S. Zhao, *J. Magn. Magn. Mater.* 424 (2017) 155.
31. W. Li, F. Wang, S. S. Feng, J. X. Wang, Z. K. Sun, B. Li, Y. H. Li, J. P. Yang, A. A. Elzatahry, Y. Y. Xia, *J. Am. Chem. Soc.* 135 (2013) 18300.
32. J. Q. Yang, X. C. Duan, Q. Qin, W. J. Zheng, *J. Mater. Chem. A* 1 (2013) 7880.
33. S. L. Kuo, N. L. Wu, *Electrochem. Solid-State Lett.* 8 (2005) A495.
34. R. Y. Wang, Q. Li, L. L. Cheng, H. L. Li, B. Y. Wang, X. S. Zhao, P. Z. Guo, *Colloids Surf., A* 457 (2014) 94.
35. P. Xiong, H. J. Huang, X. Wang, *J. Power Sources* 245 (2014) 937.
36. P. Z. Guo, Z. Li, S. B. Liu, J. Xue, G. L. Wu, H. L. Li, X. S. Zhao, *J. Mater. Sci.* 52 (2017) 5359.
37. S. L. Liu, K. W. Li, F. Yao, L. Q. Xu, G. D. Fu, *Carbohydr. Polym.* 163 (2017) 28.
38. G. X. Wang, J. Yang, J. Park, X. L. Gou, B. Wang, H. Liu, J. Yao, *J. Phys. Chem. C* 112 (2008) 8192.
39. Z. W. Wang, R. T. Downs, V. Pischedda, R. Shetty, S. K. Saxena, C. S. Zha, Y. S. Zhao, D. Schiferl, A. Waskowska, *Phys. Rev. B* 68 (2003) 185.
40. T. F. Jiao, H. Y. Guo, Q. R. Zhang, Q. M. Peng, Y. F. Tang, X. H. Yan, B. B. Li, *Sci. Rep.* 5 (2015).
41. M. Lazzeri, P. Thibaudeau, *Phys. Rev. B* 74 (2006) 2952.
42. T. F. Jiao, H. Zhao, J. X. Zhou, Q. R. Zhang, X. N. Luo, J. Hu, Q. M. Peng, X. H. Yan, *ACS Sustainable Chem. Eng.* 3 (2015) 3130.
43. P. Z. Guo, G. L. Zhang, J. Q. Yu, H. L. Li, X. S. Zhao, *Colloids Surf. A* 395 (2012) 168.
44. Y. G. Wang, Y. F. Song, Y. Y. Xia, *Chem. Soc. Rev.* 45 (2016) 5925.
45. B. Y. Wang, P. Z. Guo, H. Q. Bi, Q. Li, G. L. Zhang, R. Y. Wang, J. Q. Liu, X. S. Zhao, *Int. J. Electrochem. Sci.* 8 (2013) 8966.

© 2017 The Authors. Published by ESG (www.electrochemsci.org). This article is an open access article distributed under the terms and conditions of the Creative Commons Attribution license (<http://creativecommons.org/licenses/by/4.0/>).